5-1-2019

# An Objective Procedure for Delineating the Circumpolar Vortex

Nazla Bushra
*Louisiana State Univ, Coll Coast & Environm, Dept Oceanog & Coastal Sci*, nbushr1@lsu.edu

Robert V. Rohli
*Louisiana State Univ, Coll Coast & Environm, Dept Oceanog & Coastal Sci*, rohli@lsu.edu

Earth and Space Science

RESEARCH ARTICLE
10.1029/2019EA000590

# An Objective Procedure for Delineating the Circumpolar Vortex

**Nazla Bushra**[1] and **Robert V. Rohli**[1]

[1]Department of Oceanography & Coastal Sciences, College of the Coast & Environment, Louisiana State University and A&M College, Baton Rouge, LA, USA

**Key Points:**
- Leading edge of Northern Hemisphere's tropospheric circumpolar vortex is delineated by the steepest 500-hPa geopotential height gradient
- The new delineation represents area and circularity of the tropospheric circumpolar vortex effectively
- This technique facilitates further work on atmospheric circulation variability by objectivizing consideration of multiple vertical levels

**Correspondence to:**
N. Bushra,
nbushr1@lsu.edu

**Citation:**
Bushra, N., & Rohli, R. V. (2019). An objective procedure for delineating the circumpolar vortex. *Earth and Space Science*, *6*, 774–783. https://doi.org/10.1029/2019EA000590

Received 7 FEB 2019
Accepted 22 APR 2019
Accepted article online 29 APR 2019
Published online 15 MAY 2019
Corrected 21 JUN 2019

This article was corrected on 21 JUN 2019. See the end of the full text for details.

**Abstract** The broad-scale, steering atmospheric circulation in the Northern Hemisphere, represented by the tropospheric circumpolar vortex (CPV), is an important driver of environmental processes. The area and circularity of the CPV are analyzed hereby delineating the leading edge of the CPV at the steepest 500-hPa geopotential height gradient globally. The daily CPV area and circularity were aggregated to monthly averages for contrast with measurements identified in previous research for the overlapping period of record (1979–2001). Accuracy of representation of the CPV is assessed through correlations to air-sea teleconnections known to be associated with broad-scale, extratropical steering circulation. Correlation to monthly teleconnection indices suggests that the new method allows for improvements in the calculation of area and circularity of the 500-hPa manifestation of the CPV. These improvements justify extension of the calculation of the standardized CPV area and circularity for the 1979–2017 period of record. Results largely mirror those for the shorter time series, with the Arctic Oscillation, North Atlantic Oscillation, and Pacific-North American teleconnection showing stronger links to CPV area and circularity than El Niño–Southern Oscillation and Pacific Decadal Oscillation. Collectively, these results suggest that the use of a singular indicator isohypse and/or monthly averaged data to represent the CPV may oversimplify analyses, especially for identifying past and future longwave ridges and troughs. This finding is important because the amplitudes and positions of the undulations in the broad-scale flow exert the most important impacts on variability at both low- and high-frequency time periods.

**Plain Language Summary** This study identifies the boundary of the popularly known "polar vortex" where cold air meets much warmer air aloft over the temperate zones of Earth, using an improved, data-intensive technique that automates and objectivizes the process of identifying the polar vortex, for the 1979–2017 period. The method offers advantages over the previous techniques, as the area and waviness of the polar vortex are shown to relate better to other atmospheric features, such as circulation associated with El Niño, than the area and waviness of the polar vortex as computed in previous research. An additional advantage of the new technique is that it uses a now-available daily data set, unlike the previous polar vortex studies that calculate the polar vortex based only on monthly mean data. This research is valuable because improved identification and definition of the size and shape of the polar vortex will contribute to greater understanding of its impacts.

## 1. Introduction—The Circumpolar Vortex

The broad-scale steering atmospheric circulation is one of the most important components of the Earth-ocean-atmosphere system. Through advection of air masses and storm systems, it transfers energy, matter, and momentum between the polar and tropical parts of the Earth, thereby contributing to the energy and water balances of the planet. Therefore, delineation of both short-term fluctuations and long-term changes in this circulation is important for understanding the changing distribution of energy, matter, and momentum, both through space and time.

This hemispheric-scale steering circulation is represented by the mid-tropospheric circumpolar vortex (TCPV). While distinct from the stratospheric CPV (Waugh et al., 2017), the two TCPVs—one surrounding each pole—represent the extratropical circulation at a given time. These belts of strong quasi-west-to-east winds circumnavigate the north and south polar regions at 5–12 km in altitude. Each TCPV is situated at the steepest gradient of air temperature—at the boundary where polar air meets much warmer air at those heights. Daily changes in morphology of the TCPV represent altered distributions of energy, matter, and

momentum that comprise the variation in daily weather, such as that which produces the media-favorite "polar vortex" extreme temperature events.

Although circulation within TCPVs generally involves west-to-east flow, it bends poleward at ridges and equatorward at troughs. These ridges and troughs vary in amplitude and propagate longitudinally over time. During anomalously cold periods, the TCPVs expand equatorward, and during anomalously warm periods, they retreat poleward. At times, the TCPV is nearly circular and centered on the poles, while at other times the TCPV contains large departures from circularity and/or may be centered some distance away from the poles. Modeling research suggests that these meanders are expected to increase into the future (Peings & Magnusdottir, 2014).

Areal extent of the Northern Hemisphere's TCPV (hereafter simply referred to as CPV) has been the focus of several studies over the last several decades relating to broad-scale atmospheric circulation variability. For example, Angell and Korshover (1977) noted that the 300-hPa-defined annual-averaged CPV expanded from 1970 to 1975, while the winter vortex simultaneously contracted. Davis and Benkovic (1994) noticed an expansion of the 500-hPa-defined CPV over the 1970s and 1980s, which substantiated their previous observations (Davis & Benkovic, 1992) of expansion from 1966–1990. Interestingly, Angell (2006) observed a temporal shrinking of the 300-hPa-defined CPV of 1.5% per decade from 1963 to 2001, particularly over the Western Hemisphere. Previous work has demonstrated a link between general features of the CPV area and various environmental conditions, including air mass advection (Angell & Korshover, 1977; Diaz & Quayle, 1980; Kalnicky, 1974; Knox et al., 1988), surface temperature anomalies (Angell, 1992, 1998; Angell & Korshover, 1977, 1978, 1985; Burnett, 1993; Burnett & McNicoll, 2000; Davis & Benkovic, 1992, 1994; Frauenfeld & Davis, 2000, 2002; Markham, 1985; Rohli et al., 2005; Wrona & Rohli, 2007), sunspot activity (Angell, 2001), and precipitation (Angell, 1992; Burnett, 1993).

While some work (Thompson & Solomon, 2002) utilized vertical gradients of geopotential heights at a small number of radiosonde-based stations to index CPV behavior, most other studies described above represent the leading edge of the CPV by tracing a certain predetermined isohypse of geopotential height around the hemisphere. An important development in the definition of the CPV was the identification of a specific series of isohypses that define the center, poleward extreme, and equatorward extreme of the CPV, by month and vertical level (Frauenfeld & Davis, 2003). Since that time, several studies (Ballinger et al., 2014; Rohli et al., 2005; Wrona & Rohli, 2007) have utilized the recommended isohypses from Frauenfeld and Davis (2003).

CPV shape had only been analyzed in terms of the relative area within various quadrants about the pole (Angell, 1992, 1998, 2006) until Rohli et al. (2005) and Wrona and Rohli (2007) defined a circularity ratio ($R_c$) to characterize shape. More recently, by using an approach that identifies the length of the isohypse as an indicator of sinuosity, Vavrus et al. (2017) found that maximum waviness (i.e., meridional motion and enhanced probability of severe weather) occurs with weak flow in summer, and minimum waviness coincides with strong flow in winter.

## 2. Atmospheric Teleconnections and Hemispheric-Scale Flow

Regardless of the technique used to identify the CPV, the extent to which the CPV is an effective measure of circulation can be assessed by correlating the CPV area and $R_c$ against indices of ocean-atmospheric teleconnection patterns (Barnston & Livezey, 1987) that are known to be related to the hemispheric-scale flow. For example, the atmospheric component of the El Niño–Southern Oscillation (ENSO) phenomenon—the Southern Oscillation (SO; Bjerknes, 1969) has been shown to be related to variability in the CPV's position (Angell, 2001) and intensity of the polar front jet stream in the Pacific Ocean (Strong & Davis, 2006). El Niño events tend to be followed by shrinking of the CPV within the season (Frauenfeld & Davis, 2000) and with a three-season lag (Angell, 1992), but the eastern Pacific sector of the CPV expands during the El Niño event (Angell, 1992). Pacific variability at broader time scales, both inside and outside the tropics, is represented by the Pacific Decadal Oscillation (PDO; Newman et al., 2003). Frauenfeld and Davis (2002) emphasized on the PDO as the dominant mode influencing sea surface temperature (SST) variability in the Pacific at various time scales, thus modulating the ocean-atmosphere interaction and CPV properties at various temporal scales. Budikova (2005) implied that the CPV's physical properties are influenced by the intervention of

various PDO phases that modify surface air temperature and impact winter temperature over much of the United States.

Among extratropical teleconnections, the Pacific-North American (PNA) pattern (Wallace & Gutzler, 1981), Arctic Oscillation (AO; Thompson & Wallace, 1998), and North Atlantic Oscillation (NAO; Lamb & Peppler, 1987) have all been shown to be related to the CPV. Burnett (1993) suggested that the increased frequency of the positive mode of the PNA pattern, with its amplified ridge-trough configuration over the North Pacific Ocean and western North American mountain cordillera, may have caused the temporal increase in CPV area from 1964 to about the mid-1980s. Angell (2006) noted that although the AO cannot serve as a proxy for the CPV, the AO index is negatively correlated with CPV area. Piao et al. (2018) found that the long-term contraction of the CPV may be related to the May patterns of NAO-influenced variability.

## 3. Problem

While previous research has been valuable in quantifying the mean monthly properties and long-term changes in the CPV, especially the CPV, over time, some shortcomings exist in its identification. Specifically, the use of a predetermined isohypse of atmospheric geopotential height (and therefore atmospheric pressure and mass) a priori to represent the CPV over the entire study period is a less-than-ideal approach because weather systems move based on relative rather than absolute spatial distributions of atmospheric geopotential height (and therefore pressure and mass). Because high/low pressure systems are only "high" or "low" relative to the air around them, the assumption that a particular isohypse, such as 5,640 m for all winter months (Frauenfeld & Davis, 2003), represents the CPV's location invites caution, particularly on a daily time scale. At a minimum, days falling near the periphery of the month or season having a recommended isohypse would be represented by an increasingly inaccurate CPV. Furthermore, the previous work relied on the first-generation National Center for Atmospheric Research Reanalysis suite (Kalnay et al., 1996); use of the second-generation products (Kanamitsu et al., 2002) would allow improved spatial resolution from 5° to 2.5° with strengthened correlations to reanalysis data collected since 1979 (Saha et al., 2010), which coincides with the Satellite Era.

The purpose of this research is to introduce a technique for identifying the CPVs more effectively, represented by the sharpest gradient of atmospheric mass at the 500-hPa level using geospatial techniques with appropriate smoothing algorithms to simulate the upper-level atmospheric flow. The effectiveness of this technique will be assessed through comparison of the relationship between CPV diagnostic properties and atmospheric teleconnection patterns that are known to influence hemispheric-scale flow. Calculated values will also be compared with those derived by Wrona and Rohli (2007) using monthly data and the isohypse recommended by Frauenfeld and Davis (2003). The use of daily CPV data in this study makes it possible to address the question of appropriateness of the monthly mean CPV for the first time. After the approach is shown to be effective, the monthly time series is extended through 2017, and automated identification of the CPV can be performed in future work in identifying the daily mid-TCPV. Such use of the daily indices would allow for better understanding of the connection between changes to the steering flow and response in the form of the polar vortex and other abrupt changes of energy, matter, and momentum in the near-surface atmosphere.

## 4. Data and Methods

### 4.1. Identifying the CPV

Daily 500-hPa geopotential height data are obtained from the National Centers for Environmental Prediction/Department of Energy Reanalysis 2 project (Kanamitsu et al., 2002) for the period 1979–2017. This temporal domain is selected to include the overlapping period of the Rohli et al. (2005) and Wrona and Rohli (2007) period of record (which ended in 2001) along with subsequent years of data. For each day of analysis (1 January 1979 through 31 December 2017), the gridded 500-hPa geopotential height data set is imported into ArcGIS Desktop v10.5.1. At each 2.5° increment of longitude globally from 20°N to the North Pole, the latitude in the Northern Hemisphere having the steepest 500-hPa geopotential height gradient at that longitude is identified by iterative finite differencing across a given meridian of longitude. Then, a polygon is drawn to connect the flagged point at each of the 144 Northern Hemisphere longitudes analyzed. For each day, the procedure continues until the polygon is "closed" by connecting the last

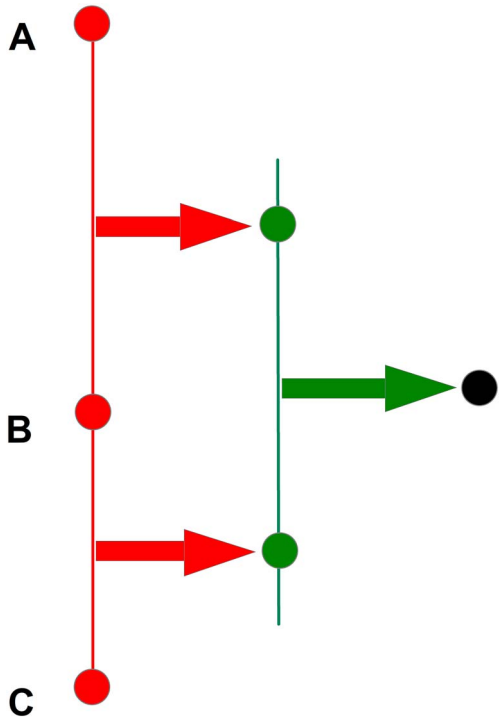


**Figure 1.** Schematic of approach for handling ties for the steepest gradient.

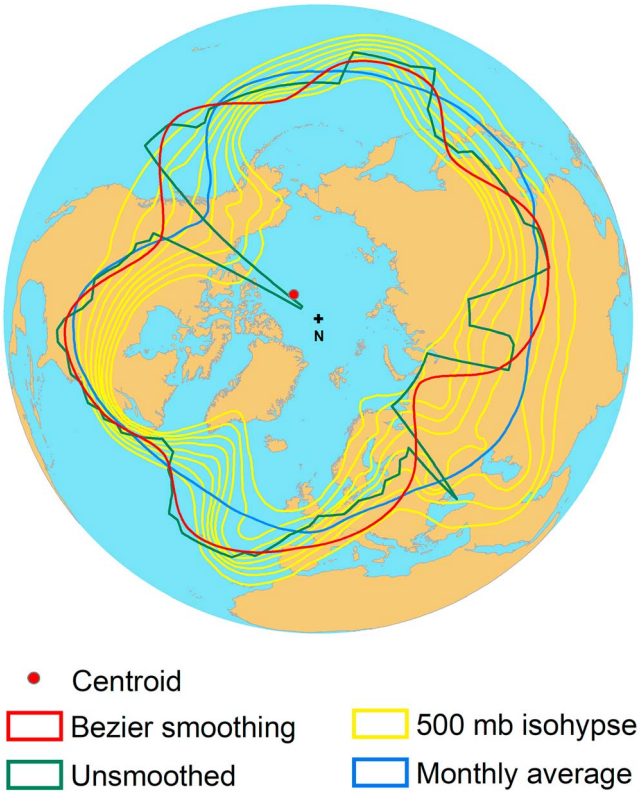


**Figure 2.** Unsmoothed and smoothed 500-hPa geopotential height, representing the circumpolar vortex on 7 January 2014, a day on which much of eastern North America experienced record low temperatures, as compared with the monthly mean value for January 2014.

flagged coordinate to the first identified coordinate. This polygon represents the unsmoothed CPV for that day.

If multiple parallels of latitude for a given meridian of longitude have the same gradient, the "pyramid" approach is employed to identify the CPV's extent. Specifically, if two latitudes along a meridian have the same sharpest gradient, then the midpoint between those latitudes is chosen; if three latitudes (A, B, and C) along a meridian have the same sharpest gradient, then the midpoint of AB and of BC is found, with the CPV demarcated at the midpoint of those two midpoints (Figure 1). If four or more points are tied, the procedure continues with the CPV demarcated at the midpoint of the midpoints of the midpoints, and so forth.

To depict the CPV as accurately and precisely as possible, the polygons representing the daily CPV were smoothed. Jekeli (2005) explains that for geopotential modeling, three types of spherical spline are generally used: (1) splines formed from polynomial and trigonometric B-splines, (2) splines constructed from radial basis functions, and (3) spherical splines based on homogeneous Bernstein-Bézier polynomials. While first two splines have implication for modeling the Earth's geoid based on assembly of geographical coordinates and considering Earth as a spheroid, the Bernstein-Bézier polynomial splines method is most suitable for any sphere-like surface (Jekeli, 2005) and is most appropriate for representing the CPV. The Bézier curve equation can be represented as follows:

$$\mathrm{B}\,(\mathrm{t}) = \sum_{\mathrm{i}=0}^{\mathrm{n}} {}_{0}n\mathrm{C}_{\mathrm{i}}(1-\mathrm{t})^{\mathrm{n}-\mathrm{i}}\mathrm{t}^{\mathrm{i}\mathrm{P}_{\mathrm{i}}},$$

where $B(t)$ is the function of parameter $t$ on a scale 0 to 1, $C$ represents the permutations, and combinations where $n$ defines the degree of the Bézier curve (i.e., whether a Bézier curve is linear, cubic, quadratic, or higher orders), and $P$ is the number of anchor and control points. The cubic Bézier curve is applied here to smooth the CPV boundary. Figure 2 presents an example of the unsmoothed polygon, with its Bézier curve and the 500-hPa isohypse, on 7 January 2014, a day with an unusually deep trough over much of central and eastern North America commonly described in the popular media as a polar vortex. The centroid of the smoothed polygon barely falls inside the unsmoothed polygon.

The calculated daily CPV also initially included unusual shapes for a small percentage of days. These CPVs presented computational challenges, including perforations (i.e., "donuts") of colder air surrounded spuriously by warmer air and proruptions (i.e., "snakes") of a narrow zone of colder air wrapped spuriously equatorward of warmer air and required further analysis. These donuts and snakes were identified, removed, and quality controlled, with the revised CPV demarcated by the leading edge of the perforation, which proved in test cases to represent the CPV most realistically when compared to the temperature and atmospheric teleconnection patterns.

### 4.2. Calculating CPV Area and Circularity Ratio ($R_c$)

Once the daily 500-hPa CPVs were identified, diagnostics were calculated. To do this, the mapped polygon was projected into the Lambert's equal area (i.e., equivalent) map projection, and the area enclosed within the polygon was calculated. Lambert's projection has been found to be useful for areas that have near-equal north-south and east-west dimensions

**Table 1**
*Sources of Atmospheric Teleconnection Indices*

| Teleconnection | Source |
|---|---|
| El Niño/Southern Oscillation (daily) | SOI: https://data.qld.gov.au/dataset/the-southern-oscillation-index-soi-daily Niño 3.4: http://www.cpc.noaa.gov/data/indices/ |
| Pacific-North American Pattern (daily) | http://www.cpc.ncep.noaa.gov/products/precip/CWlink/daily_ao_index/teleconnections.shtml |
| Arctic Oscillation (daily) | http://www.cpc.ncep.noaa.gov/products/precip/CWlink/daily_ao_index/teleconnections.shtml |
| North Atlantic Oscillation (daily) | http://www.cpc.ncep.noaa.gov/products/precip/CWlink/daily_ao_index/teleconnections.shtml |
| Pacific Decadal Oscillation (monthly only) | https://www.ncdc.noaa.gov/teleconnections/pdo/ |

(Robinson et al., 1984), as is the case for the CPV. Then the mapped polygon was projected into the conformal (i.e., equal shape) polar stereographic projection to calculate the perimeter of the CPV. As in Rohli et al. (2005) and Wrona and Rohli (2007), the "circularity ratio" ($R_c$), a measure of shape borrowed from fluvial geomorphology (Chorley et al., 1984), was used to index circularity of the CPV and was calculated as

$$R_c = \frac{A}{A_c}, \tag{1}$$

where $A$ represents the area enclosed within the CPV and $A_c$ represents the area of the circle with the same perimeter as the CPV on that day. Thus, theoretically, $R_c$ can vary between 0 and 1, with $R_c$ being proportional to the circularity of the westerly flow in the CPV. Small values of $R_c$ suggest amplified and/or more numerous longwave ridges and troughs. Because O'Sullivan and Unwin (2003) recommended

$$R_c = \sqrt{\frac{A}{A_c}} \tag{2}$$

comparisons of the methods were run, with the calculation that yields the most significant Pearson product-moment correlations to six common teleconnection indices being implemented in all subsequent analyses. The teleconnection indices used were the SO index (SOI; Bunge & Clarke, 2009; Können et al., 1998; Ropelewski & Jones, 1987) and Niño3.4 index (Bunge & Clarke, 2009; Ren & Jin, 2011) representing ENSO, along with indices representing the PNA pattern, AO, NAO, and PDO, the latter of which is only available at the monthly time scale. Teleconnection indices were downloaded from the sources listed in Table 1. The process of computing area and the "best" $R_c$ was repeated for the 8,401 days between 1 January 1979 and 31 December 2001. Daily areas and $R_c$ were then statistically standardized ($n = 23$) for that day, so that the CPV properties could be compared across days, months, and seasons. For comparison with Wrona and Rohli (2007), the daily-standardized area and $R_c$ were aggregated to monthly mean standardized area and $R_c$.

Because Wrona and Rohli (2007) only analyzed monthly Pearson correlations for December, January, February, April, July, and October, only those months were used for comparison. Moreover, data for the July PNA index were unavailable, as the PNA pattern is not prominent in the summer months (Barnston & Livezey, 1987). As in Wrona and Rohli (2007), associations between the CPV properties (area and $R_c$) and regional-scale teleconnection indices are presumed to imply that the CPV ridges and troughs are forced by the relevant teleconnection. In reality, interactions exist between multiple teleconnections, including some that are not analyzed here, such as the West Pacific (Wallace & Gutzler, 1981) and tropical Northern Hemisphere (Mo & Livezey, 1986) patterns. While such influences would remain undetected in this analysis, it is highly likely that the major influence will be captured by at least one of the indices for the six teleconnections known to produce the largest variability in Northern Hemisphere flow.

## 5. Results and Discussion

### 5.1. Validation of the Approach

Results suggest that the new approach identifies stronger relationships to the teleconnection indices, compared to those reported for the same time period by Wrona and Rohli (2007). Specifically, 12 (12)

**Table 2**
*Comparison of Pearson Correlations of the Area and Circularity Ratio ($R_c$) of Monthly Circumpolar Vortex Versus Several Atmospheric and Sea Surface Temperature Indices, Between Present Study and Wrona and Rohli (2007)*

| | Present study | | | | | | | | | | | |
|---|---|---|---|---|---|---|---|---|---|---|---|---|
| | AO | | NAO | | PNA | | PDO | | SOI | | NIÑO3.4 | |
| Month | *r* Value | *p* Value | *r* Value | *p* Value | *r* Value | *p* Value | *r* Value | *p* Value | *r* Value | *p* Value | *r* Value | *p* Value |
| Area | | | | | | | | | | | | |
| Dec | **−0.454** | **0.030** | **−0.397** | **0.023** | 0.240 | 0.270 | −0.041 | 0.852 | **0.360** | **0.046** | −0.116 | 0.598 |
| Jan | **−0.540** | **0.042** | −0.289 | 0.078 | 0.210 | 0.337 | −0.005 | 0.981 | −0.270 | 0.089 | 0.116 | 0.599 |
| Feb | **−0.678** | **<0.000** | **−0.530** | **0.009** | −0.204 | 0.351 | −0.139 | 0.527 | **0.340** | **0.032** | **−0.669** | **<0.001** |
| Apr | **−0.567** | **0.005** | 0.034 | 0.877 | 0.249 | 0.252 | 0.211 | 0.332 | −0.205 | 0.348 | 0.099 | 0.653 |
| Jul | **−0.631** | **0.001** | **−0.466** | **0.027** | ... | | 0.159 | 0.469 | −0.077 | 0.726 | −0.012 | 0.957 |
| Oct | −0.221 | 0.312 | **−0.358** | **0.043** | −0.103 | 0.639 | −0.107 | 0.626 | −0.027 | 0.903 | −0.240 | 0.269 |
| $R_c$ | | | | | | | | | | | | |
| Dec | **0.541** | **0.008** | **0.125** | **0.071** | **−0.375** | **0.048** | **−0.416** | **0.048** | −0.264 | 0.095 | 0.157 | 0.475 |
| Jan | 0.152 | 0.488 | 0.250 | 0.091 | **−0.653** | **<0.000** | −0.304 | 0.082 | **0.523** | **0.010** | **−0.360** | **0.049** |
| Feb | 0.074 | 0.736 | −0.182 | 0.406 | **−0.423** | **0.044** | −0.163 | 0.457 | −0.006 | 0.979 | −0.067 | 0.763 |
| Apr | **0.629** | **0.001** | 0.178 | 0.416 | −0.295 | 0.172 | −0.285 | 0.079 | 0.243 | 0.264 | −0.186 | 0.396 |
| Jul | **0.630** | **0.001** | **0.622** | **0.002** | ... | | −0.293 | 0.076 | 0.286 | 0.650 | −0.166 | 0.448 |
| Oct | **0.551** | **0.006** | 0.353 | 0.098 | −0.181 | 0.409 | −0.374 | 0.079 | 0.248 | 0.254 | 0.004 | 0.986 |

*Note*. Correlations significant at $\alpha < 0.05$ are shown in bold. AO = Arctic Oscillation; NAO = North Atlantic Oscillation; PNA = Pacific-North American; PDO = Pacific Decadal Oscillation; SOI = Southern Oscillation index.

significant ($\alpha = 0.05$) correlations to the area ($R_c$) are identified, compared with 10 (6) by Wrona and Rohli (2007), for the 6 months analyzed (Table 2). In general, the similarity of the magnitudes and signs correlations in the matrix (other than being stronger in the present study) between the present study and that of Wrona and Rohli (2007) corroborates the findings.

The AO has the strongest and most significant relationship to both CPV area and $R_c$, with consistent results to those reported by Wrona and Rohli (2007), as shown in Table 2. Specifically, in each winter month, and also in April and July, the warm (cold) phase of the AO is linked to smaller and more circular (larger and less circular) CPV. This result supports the theoretical arguments of a smaller (larger) CPV when the midlatitudes are warmed (cooled), as is the case in a positive (negative) AO regime. The strengthened (weakened) midlatitude geopotential height gradient during a positive (negative) AO (Thompson et al., 2000) also induces a more (less) circular CPV, with the thermal conditions of the warm (cold) phase tending to shrink (expand) the CPV. Likewise, with its characteristic increase in zonality (meridionality), the positive (negative) phase of the NAO is linked to smaller (larger) and more (less) circular CPV but with fewer months displaying the significant relationship. Because the AO and NAO are related to each other (Marshall et al., 2001; Rogers & McHugh, 2002), the similarity of the correlations between the NAO and CPV also corroborates the findings.

While no significant relationships to area were found, the PNA pattern also has a strong relationship to the CPV $R_c$. As would be expected, amplification (deamplification) of the ridge-trough configuration is associated with significantly lower (higher) $R_c$ in each of the three winter months. The implication is that amplification of the Rossby wave train across a significant part of the hemisphere drives amplifications of adjacent Rossby ridge-trough configurations in response, while altering the net CPV area insignificantly. Another implication is that the smoothing algorithm introduced here performed well, because it preserved the relationship that is known with most certainty to exist; waviness (or lack thereof) in the PNA pattern should coincide with low (or high) $R_c$. Furthermore, results again corroborate those of Wrona and Rohli (2007), but the method used by the latter allowed only the core winter month of January to display statistically significant results.

As suggested in previous research (Angell, 1992; Frauenfeld & Davis, 2003), ENSO also shows some relationship to the CPV area and $R_c$, as identified in this research. Specifically, a larger (smaller) CPV occurs during the La Niña (El Niño) phase, with significant associations occurring in December and February (as defined by the SOI, which defines the El Niño phase as negative values) or February only (as defined by Niño3.4,

**Table 2** *(continued)*

| | Wrona and Rohli (2007) | | | | | | | | | | | |
|---|---|---|---|---|---|---|---|---|---|---|---|---|
| | AO | | NAO | | PNA | | PDO | | SOI | | NIÑO3.4 | |
| Month | *r* Value | *p* Value | *r* Value | *p* Value | *r* Value | *p* Value | *r* Value | *p* Value | *r* Value | *p* Value | *r* Value | *p* Value |
| Area | | | | | | | | | | | | |
| Dec | **−0.709** | **<0.000** | **−0.527** | **0.010** | **0.708** | **<0.000** | 0.356 | 0.065 | 0.076 | 0.730 | −0.012 | 0.960 |
| Jan | **−0.649** | **<0.000** | −0.412 | 0.051 | 0.333 | 0.120 | 0.368 | 0.061 | −0.267 | 0.219 | 0.339 | 0.112 |
| Feb | **−0.647** | **<0.000** | **−0.562** | **0.005** | 0.218 | 0.317 | 0.276 | 0.203 | −0.112 | 0.612 | 0.119 | 0.588 |
| Apr | **−0.594** | **0.003** | **−0.415** | **0.049** | 0.200 | 0.360 | 0.419 | 0.052 | −0.198 | 0.365 | 0.380 | 0.074 |
| Jul | −0.386 | 0.069 | 0.025 | 0.908 | | | 0.344 | 0.136 | **−0.549** | **0.007** | **0.586** | **0.003** |
| Oct | −0.289 | 0.181 | −0.262 | 0.227 | 0.296 | 0.170 | 0.366 | 0.086 | −0.087 | 0.693 | −0.117 | 0.594 |
| $R_c$ | | | | | | | | | | | | |
| Dec | **0.491** | **0.017** | 0.526 | 0.010 | −0.398 | 0.060 | −0.144 | 0.512 | −0.138 | 0.529 | 0.332 | 0.121 |
| Jan | 0.214 | 0.328 | **0.427** | **0.042** | **−0.660** | **<0.000** | −0.289 | 0.180 | 0.050 | 0.821 | −0.004 | 0.984 |
| Feb | 0.142 | 0.517 | −0.126 | 0.565 | −0.254 | 0.242 | −0.292 | 0.176 | 0.003 | 0.99 | −0.045 | 0.838 |
| Apr | 0.163 | 0.457 | 0.393 | 0.064 | −0.129 | 0.558 | −0.261 | 0.230 | 0.147 | 0.502 | −0.174 | 0.430 |
| Jul | 0.057 | 0.797 | 0.253 | 0.244 | ... | | 0.294 | 0.174 | 0.068 | 0.758 | 0.117 | 0.594 |
| Oct | **0.445** | **0.033** | 0.114 | 0.604 | −0.393 | 0.063 | **−0.588** | **0.003** | 0.252 | 0.247 | −0.332 | 0.121 |

which represents the El Niño phase through positive SST anomalies). The implication is that the polar front is shifted anomalously southward (northward) by the presence of colder (warmer) than normal winters during La Niña (El Niño). Notably, the insignificant correlations in other months are often of opposite signs. Unlike the cases for AO, NAO, and PNA pattern, the ENSO relationships described here were undetected by Wrona and Rohli (2007); instead, they found a relationship only in July (Table 2), but because of the known strength of ENSO associations in winter, our results here seem more plausible.

Finally, a negative relationship between the PDO and $R_c$ was observed but only in December (Table 2). This result is reasonable, because the positive (negative), or warm (cold), phase of the PDO (which is characterized by a long-term (20–30 years) periodic oscillations in the tropical central and eastern Pacific Ocean) creates greater (lesser) undulation in the ridges and troughs of the CPV and thus decreases (increases) the NHTCPV's circularity (Newman et al., 2003). Because of the long-term periodic nature of the PDO, this result should be interpreted with caution, as a 23-year study period may not represent the true nature of the PDO-induced variability. Moreover, this relationship was undetected by Wrona and Rohli (2007), who instead found a (negative) relationship only in October.

### 5.2. Extension of the Time Series

With confidence in the approach established, the time series is extended to all 12 months of the January 1979 to December 2017 period. Many, but not all, of the patterns that emerge are similar to those of the shorter time series. The AO remains the teleconnection with the most direct correlation to the CPV. In 9 of the 12 months, a warm (cold) AO is linked to a smaller (larger) CPV (Table 3). In contrast to the 1979–2001 period, this correlation is somewhat weaker in winter than the other months, with 2 of the 3 months lacking a significant relationship are January and February. The findings for $\boldsymbol{R_c}$ also echo those for the shorter time series, as 10 of the 12 months show that warm (cold) AO is linked to a more (less) circular CPV. Interestingly, again January and February are the months in which this relationship is not significant.

The linkages to the NAO also largely echo the results from the 1979–2001 period and corroborate relationships between the NAO and AO (Table 3). Four months (March, June, July, and October) have CPV areas with significant positive relationships to the NAO, and only 1 month (January) shows a significant negative correlation. Three of the months showing positive relationships to area (June, July, and October) also show a positive link between the NAO and $\boldsymbol{R_c}$. Thus, a positive (negative) NAO is associated with smaller (larger) and more (less) circular CPV, at least for June, July, and October.

While the PNA pattern showed no links to the CPV area in the shorter time series, expansion of the number of years of analysis causes the PNA pattern to display significantly positive relationships to area, in

**Table 3**
*Pearson Correlations of the Area and Circularity Ratio ($R_c$) of All Months Circumpolar Vortex Versus Several Atmospheric and Sea Surface Temperature Indices for the Extended Time Period (1979–2017)*

| | AO | | NAO | | PNA | | PDO | | SOI | | NIÑO3.4 | |
|---|---|---|---|---|---|---|---|---|---|---|---|---|
| Month | *r* Value | *p* Value | *r* Value | *p* Value | *r* Value | *p* Value | *r* Value | *p* Value | *r* Value | *p* Value | *r* Value | *p* Value |
| Area | | | | | | | | | | | | |
| Winter | | | | | | | | | | | | |
| Dec | **−0.325** | **0.043** | −0.061 | 0.712 | **0.462** | **0.003** | 0.043 | 0.793 | 0.327 | 0.064 | −0.189 | 0.249 |
| Jan | −0.034 | 0.835 | **0.356** | **0.026** | 0.138 | 0.401 | −0.056 | 0.733 | −0.154 | 0.350 | 0.287 | 0.077 |
| Feb | 0.002 | 0.990 | 0.286 | 0.078 | 0.120 | 0.467 | −0.164 | 0.317 | 0.130 | 0.430 | −0.216 | 0.186 |
| Spring | | | | | | | | | | | | |
| Mar | **−0.378** | **0.018** | **−0.364** | **0.023** | 0.090 | 0.587 | 0.052 | 0.754 | 0.002 | 0.989 | −0.259 | 0.111 |
| Apr | **−0.517** | **0.001** | 0.058 | 0.724 | 0.218 | 0.183 | 0.239 | 0.143 | −0.190 | 0.246 | 0.180 | 0.272 |
| May | **−0.524** | **0.001** | −0.221 | 0.177 | 0.044 | 0.790 | 0.038 | 0.817 | −0.193 | 0.238 | −0.178 | 0.278 |
| Summer | | | | | | | | | | | | |
| Jun | **−0.495** | **0.001** | **−0.409** | **0.010** | 0.198 | 0.227 | 0.147 | 0.373 | −0.275 | 0.090 | −0.102 | 0.535 |
| Jul | **−0.712** | **<0.000** | **−0.503** | **0.001** | 0.210 | 0.201 | 0.183 | 0.266 | −0.235 | 0.150 | 0.153 | 0.353 |
| Aug | −0.398 | 0.055 | 0.175 | 0.287 | **0.656** | **<0.000** | 0.011 | 0.948 | −0.067 | 0.684 | −0.107 | 0.515 |
| Autumn | | | | | | | | | | | | |
| Sep | **−0.541** | **0.000** | 0.120 | 0.468 | **0.418** | **0.008** | −0.055 | 0.737 | 0.274 | 0.092 | −0.170 | 0.302 |
| Oct | **−0.403** | **0.048** | **−0.352** | **0.028** | 0.077 | 0.642 | −0.045 | 0.786 | −0.041 | 0.802 | −0.196 | 0.231 |
| Nov | **−0.493** | **0.001** | −0.173 | 0.292 | **0.382** | **0.016** | **0.317** | **0.049** | 0.031 | 0.852 | 0.115 | 0.487 |
| $R_c$ | | | | | | | | | | | | |
| Winter | | | | | | | | | | | | |
| Dec | **0.401** | **0.011** | 0.090 | 0.586 | **−0.456** | **0.004** | −0.288 | 0.076 | −0.254 | 0.118 | 0.190 | 0.248 |
| Jan | 0.289 | 0.074 | 0.076 | 0.645 | **−0.577** | **<0.000** | −0.243 | 0.136 | **0.421** | **0.008** | **−0.491** | **0.043** |
| Feb | 0.302 | 0.052 | 0.016 | 0.921 | **−0.503** | **0.001** | −0.127 | 0.442 | 0.149 | 0.365 | −0.120 | 0.466 |
| Spring | | | | | | | | | | | | |
| Mar | **0.434** | **0.006** | 0.216 | 0.187 | **−0.541** | **<0.000** | **−0.493** | **0.001** | 0.216 | 0.187 | 0.265 | 0.103 |
| Apr | **0.606** | **<0.000** | 0.099 | 0.548 | **−0.380** | **0.017** | **−0.330** | **0.040** | 0.221 | 0.175 | −0.252 | 0.122 |
| May | **0.570** | **<0.000** | 0.271 | 0.095 | **−0.370** | **0.021** | −0.165 | 0.316 | 0.204 | 0.213 | 0.038 | 0.818 |
| Summer | | | | | | | | | | | | |
| Jun | **0.489** | **0.002** | **0.338** | **0.035** | **−0.405** | **0.011** | −0.231 | 0.157 | 0.220 | 0.179 | 0.035 | 0.832 |
| Jul | **0.731** | **<0.000** | **0.604** | **<0.000** | **−0.363** | **0.023** | −0.253 | 0.120 | 0.284 | 0.080 | −0.262 | 0.108 |
| Aug | **0.502** | **0.001** | −0.027 | 0.868 | **−0.590** | **<0.000** | 0.064 | 0.699 | 0.087 | 0.599 | 0.112 | 0.496 |
| Autumn | | | | | | | | | | | | |
| Sep | **0.503** | **0.001** | −0.172 | 0.294 | **−0.344** | **0.032** | −0.052 | 0.753 | **−0.330** | **0.040** | 0.157 | 0.341 |
| Oct | **0.555** | **<0.000** | **0.604** | **<0.000** | −0.277 | 0.088 | 0.021 | 0.900 | 0.085 | 0.608 | 0.068 | 0.680 |
| Nov | **0.594** | **<0.000** | 0.294 | 0.069 | **−0.664** | **<0.000** | **−0.391** | **0.014** | −0.092 | 0.578 | −0.167 | 0.311 |

*Note*. Correlations significant at $\alpha < 0.05$ are shown in bold. AO = Arctic Oscillation; NAO = North Atlantic Oscillation; PNA = Pacific-North American; PDO = Pacific Decadal Oscillation; SOI = Southern Oscillation index.

December, August, September, and November (Table 3). While at first glance, this result might suggest a possible bias in the smoothing algorithm, in which adjacent troughs might have been connected instead of separated by a ridge, the absence of such a relationship in the shorter time series, along with the presence of significant negative relationships between the PNA index and $\boldsymbol{R_c}$ in 11 of the 12 months, suggests that the smoothing algorithm succeeded.

Looking to the Pacific Ocean, as was the case for the shorter time series, the PDO displays few relationships to the CPV (Table 3). Only November has a correlation with both area and $\boldsymbol{R_c}$, with a positive (negative) PDO coincident with larger (smaller) and less (more) circular CPV. March and April share this same PDO-$\boldsymbol{R_c}$ relationship but display no significant link between PDO and area.

ENSO shows a weaker relationship to the CPV than occurred over the shorter time series. None of the relationships between CPV area and ENSO that appeared in the 1979–2001 period were evident over the 1979–2017 period (compare Tables 2 and 3). However, the relationships to $\boldsymbol{R_c}$ are largely the same over the two time series, with only January displaying a significant link between ENSO, as defined by both the SOI and Niño3.4 indices. El Niño (La Niña) in January is associated with a less (more) circular CPV. September, which was not analyzed in the shorter time series analysis because it was not analyzed by

Wrona and Rohli (2007), also shows some evidence of an ENSO link to $\boldsymbol{R_c}$ but only when ENSO is defined by SOI and in the opposite direction as January; El Niño (La Niña) in September is associated with a more (less) circular CPV.

## 6. Summary and Conclusions

This research introduces an effective, objective method for identifying the TCPV. Results suggest that the area of the CPV as calculated here offers improvements over those of Wrona and Rohli (2007) as evidenced by significance of correlations to the major modes of hemispheric-scale variability in the form of both tropical and extratropical atmospheric teleconnections. The technique also improves the identification of circularity of the CPV substantially. Given the demonstrated improvement of this index, it was implemented for all 12 months of the period of available data (1979–2017).

The CPV is most closely linked to variability associated with the AO and NAO, followed by the PNA pattern, ENSO, and finally the PDO. These results, while not surprising, have implications for forecasting at seasonal time scales and beyond. Now that this technique has been validated by comparison to previous work at the monthly scale of analysis and the time series of the standardized CPV area and circularity has been updated, future research should investigate the practicality of delineating diurnal features of the CPV as identified herein.

The technique introduced here is a rich source of future studies of atmospheric circulation variability because it permits the consideration of multiple vertical levels, for continuous updating of the CPVs diagnostic features on a near-real-time basis. For example, such work will allow for identification of a signal of global climatic change in the upper-level flow. A warming planet should cause impacts that ripple through the troposphere. Lack of such a signal could either indicate impacts that do not resonate effectively or impacts that are yet to be felt through the troposphere. Furthermore, the technique allows future research on the identification for the identification of changes in the baroclinicity of the upper-level steering flow. Such changes could alter the vertical wind shear that would affect the development of midlatitude storm systems. The improved understanding of the drivers of such broad-scale flow could have important implications for protecting life and property.

**Acknowledgments**
The authors gratefully acknowledge the financial support of Louisiana State University's Economic Development Assistantship program. The data used in this research, which characterizes the NHCPV properties (i.e., CPV centroid location, area, and circularity [CLAC]) are generated as described in more detail in section , from the gridded data set obtained from the National Centers for Environmental Prediction (NCEP)/Department of Energy (DOE) Reanalysis 2 project. The data are available at https://www.esrl.noaa.gov/psd/data/gridded/data.ncep.reanalysis2.pressure.html. The data sources for the air-sea teleconnection indices are listed in Table 1 in section 4.

## References

Angell, J. K. (1992). Relation between 300-mb north polar vortex and equatorial SST, QBO, and sunspot number and the record contraction of the vortex in 1988-89. *Journal of Climate*, *5*(1), 22–29. https://doi.org/10.1175/1520-0442(1992)005<0022:RBMNPV>2.0.CO;2

Angell, J. K. (1998). Contraction of the 300 mbar north circumpolar vortex during 1963–1997 and its movement into the eastern hemisphere. *Journal of Geophysical Research-Atmospheres*, *103*(D20), 25,887–25,893. https://doi.org/10.1029/98JD02451

Angell, J. K. (2001). Relation of size and displacement of the 300 mbar north circumpolar vortex to QBO, El Niño, and sunspot number, 1963—2000. *Journal of Geophysical Research-Atmospheres*, *106*(D23), 31,787–31,794. https://doi.org/10.1029/2001JD000473

Angell, J. K. (2006). Changes in the 300-mb North circumpolar vortex, 1963—2001. *Journal of Climate*, *19*(12), 2984–2994. https://doi.org/10.1175/JCLI3778.1

Angell, J. K., & Korshover, J. (1977). Variation in size and location of 300 mb north circumpolar vortex between 1963 and 1975. *Monthly Weather Review*, *105*(1), 19–25. https://doi.org/10.1175/1520-0493(1977)105<0019:VISALO>2.0.CO;2

Angell, J. K., & Korshover, J. (1978). Expanded north circumpolar vortex of 1976 and winter of 1976-1977, and attendant vortex displacement. *Monthly Weather Review*, *106*(1), 137–142. https://doi.org/10.1175/1520-0493(1978)106<0137:TENCVO>2.0.CO;2

Angell, J. K., & Korshover, J. (1985). Displacements of the north circumpolar vortex during El-Niño, 1963-83. *Monthly Weather Review*, *113*(9), 1627–1630. https://doi.org/10.1175/1520-0493(1985)113<1627:DOTNCV>2.0.CO;2

Ballinger, T. J., Allen, M. J., & Rohli, R. V. (2014). Spatiotemporal analysis of the January Northern Hemisphere circumpolar vortex over the contiguous United States. *Geophysical Research Letters*, *41*, 3602–3608. https://doi.org/10.1002/2014GL060285

Barnston, A. G., & Livezey, R. E. (1987). Classification, seasonality and persistence of low-frequency atmospheric circulation patterns. *Monthly Weather Review*, *115*(6), 1083–1126. https://doi.org/10.1175/1520-0493(1987)115<1083:CSAPOL>2.0.CO;2

Bjerknes, J. (1969). Atmospheric teleconnections from the equatorial Pacific. *Monthly Weather Review*, *97*(3), 163–172. https://doi.org/10.1175/1520-0493(1969)097<0163:ATFTEP>2.3.CO;2

Budikova, D. (2005). Impact of the Pacific Decadal Oscillation on relationships between temperature and the Arctic Oscillation in the USA in winter. *Climate Research*, *29*(3), 199–208. https://doi.org/10.3354/cr029199

Bunge, L., & Clarke, A. J. (2009). A verified estimation of the El Niño index Niño-3.4 since 1877. *Journal of Climate*, *22*(14), 3979–3992. https://doi.org/10.1175/2009JCLI2724.1

Burnett, A. W. (1993). Size variations and long-wave circulation within the January northern-hemisphere circumpolar vortex—1946–89. *Journal of Climate*, *6*(10), 1914–1920. https://doi.org/10.1175/1520-0442(1993)006<1914:SVALWC>2.0.CO;2

Burnett, A. W., & McNicoll, A. R. (2000). Interannual variations in the Southern Hemisphere winter circumpolar vortex: Relationships with the semiannual oscillation. *Journal of Climate*, *13*(5), 991–999. https://doi.org/10.1175/1520-0442(2000)013<0991:IVITSH>2.0.CO;2

Chorley, R. J., Schumm, S. A., & Sugden, D. E. (1984). *Geomorphology*. London, New York: Metheun & Co. ISBN 0 416 32590 4

Davis, R. E., & Benkovic, S. R. (1992). Climatological variations in the northern-hemisphere circumpolar vortex in January. *Theoretical and Applied Climatology*, *46*(2–3), 63–73. https://doi.org/10.1007/BF00866086

Davis, R. E., & Benkovic, S. R. (1994). Spatial and temporal variations of the January circumpolar vortex over the Northern Hemisphere. *International Journal of Climatology*, *14*(4), 415–428. https://doi.org/10.1002/joc.3370140406

Diaz, H. F., & Quayle, R. G. (1980). An analysis of the recent extreme winters in the contiguous United-States. *Monthly Weather Review*, *108*(6), 687–699. https://doi.org/10.1175/1520-0493(1980)108<0687:AAOTRE>2.0.CO;2

Frauenfeld, O. W., & Davis, R. E. (2000). The influence of El Niño-Southern Oscillation events on the Northern Hemisphere 500 hPa circumpolar vortex. *Geophysical Research Letters*, *27*(4), 537–540. https://doi.org/10.1029/1999GL010996

Frauenfeld, O. W., & Davis, R. E. (2002). Midlatitude circulation patterns associated with decadal and interannual Pacific Ocean variability. *Geophysical Research Letters*, *29*(24), 2221. https://doi.org/10.1029/2002GL015743

Frauenfeld, O. W., & Davis, R. E. (2003). Northern Hemisphere circumpolar vortex trends and climate change implications. *Journal of Geophysical Research-Atmospheres*, *108*(D14), 4423. https://doi.org/10.1029/2002JD002958

Jekeli, C. (2005). Spline representations of functions on a sphere for geopotential modeling (Report No. 475, pp. 37). Department of Civil and Environmental Engineering and Geodetic Science, The Ohio State University.

Kalnay, E., Kanamitsu, M., Kistler, R., Collins, W., Deaven, D., Gandin, L., et al. (1996). The NCEP/NCAR 40-year reanalysis project. *Bulletin of the American Meteorological Society*, *77*(3), 437–471. https://doi.org/10.1175/1520-0477(1996)077<0437:TNYRP>2.0.CO;2

Kalnicky, R. A. (1974). Climatic change since 1950. *Annals of the Association of American Geographers*, *64*(1), 100–112. https://doi.org/10.1111/j.1467-8306.1974.tb00957.x

Kanamitsu, M., Ebisuzaki, W., Woollen, J., Yang, S. K., Hnilo, J. J., Fiorino, M., & Potter, G. L. (2002). NCEP-DOE AMIP-II Reanalysis (R-2). *Bulletin of the American Meteorological Society*, *83*(11), 1631–1644. https://doi.org/10.1175/BAMS-83-11-1631

Knox, J. L., Higuchi, K., Shabbar, A., & Sargent, N. E. (1988). Secular variation of Northern Hemisphere 50 kPa geopotential height. *Journal of Climate*, *1*(5), 500–511. https://doi.org/10.1175/1520-0442(1988)001<0500:SVONHK>2.0.CO;2

Können, G. P., Jones, P. D., Kaltofen, M. H., & Allan, R. J. (1998). Pre-1866 extensions of the Southern Oscillation Index using early Indonesian and Tahitian meteorological readings. *Journal of Climate*, *11*(9), 2325–2339. https://doi.org/10.1175/1520-0442(1998)011<2325:PEOTSO>2.0.CO;2

Lamb, P. J., & Peppler, R. A. (1987). North Atlantic Oscillation: Concept and an Application. *Bulletin of the American Meteorological Society*, *68*(10), 1218–1225. https://doi.org/10.1175/1520-0477(1987)068<1218:NAOCAA>2.0.CO;2

Markham, C. G. (1985). A quick and direct method for estimating mean monthly global temperatures from 500 mb data. *The Professional Geographer*, *37*(1), 72–74. https://doi.org/10.1111/j.0033-0124.1985.00072.x

Marshall, J., Kushnir, Y., Battisti, D., Chang, P., Czaja, A., Dickson, R., et al. (2001). North Atlantic climate variability: Phenomena, impacts and mechanisms. *International Journal of Climatology*, *21*(15), 1863–1898. https://doi.org/10.1002/joc.693

Mo, K. C., & Livezey, R. E. (1986). Tropical-extratropical geopotential height teleconnections during the Northern Hemisphere winter. *Monthly Weather Review*, *114*(12), 2488–2515. https://doi.org/10.1175/1520-0493(1986)114<2488:TEGHTD>2.0.CO;2

Newman, M., Compo, G. P., & Alexander, M. A. (2003). ENSO-forced variability of the Pacific Decadal Oscillation. *Journal of Climate*, *16*(23), 3853–3857. https://doi.org/10.1175/1520-0442(2003)016<3853:EVOTPD>2.0.CO;2

O'Sullivan, D., & Unwin, D. J. (2003). *Geographic Information Analysis*. Hoboken, NJ: Wiley.

Peings, Y., & Magnusdottir, G. (2014). Response of the wintertime northern hemisphere atmospheric circulation to current and projected Arctic sea ice decline: A numerical study with CAM5. *Journal of Climate*, *27*(1), 244–264. https://doi.org/10.1175/JCLI-D-13-00272.1

Piao, J. L., Chen, W., Chen, S. F., & Wei, K. (2018). Intensified impact of North Atlantic Oscillation in May on subsequent July Asian inland plateau precipitation since the late 1970s. *International Journal of Climatology*, *38*(5), 2605–2612. https://doi.org/10.1002/joc.5332

Ren, H. L., & Jin, F. F. (2011). Niño indices for two types of ENSO. *Geophysical Research Letters*, *38*, L04704. https://doi.org/10.1029/2010GL046031

Robinson, A. H., Sale, R. D., Morrison, J. L., & Muehrcke, P. C. (1984). *Elements of Cartography*, (5th ed.). Toronto: John Wiley & Sons.

Rogers, J., & McHugh, M. (2002). On the separability of the North Atlantic oscillation and Arctic oscillation. *Climate Dynamics*, *19*(7), 599–608. https://doi.org/10.1007/s00382-002-0247-7

Rohli, R. V., Wrona, K. M., & McHugh, M. J. (2005). January northern hemisphere circumpolar vortex variability and its relationship with hemispheric temperature and regional teleconnections. *International Journal of Climatology*, *25*(11), 1421–1436. https://doi.org/10.1002/joc.1204

Ropelewski, C. F., & Jones, P. D. (1987). An extension of the Tahiti–Darwin southern oscillation index. *Monthly Weather Review*, *115*(9), 2161–2165. https://doi.org/10.1175/1520-0493(1987)115<2161:AEOTTS>2.0.CO;2

Saha, S., Moorthi, S., Pan, H.-L., Wu, X., Wang, J., Nadiga, S., et al. (2010). The NCEP climate forecast system reanalysis. *Bulletin of the American Meteorological Society*, *91*(8), 1015–1058. https://doi.org/10.1175/2010BAMS3001.1

Strong, C., & Davis, R. E. (2006). Variability in the altitude of fast upper tropospheric winds over the Northern Hemisphere during winter. *Journal of Geophysical Research – Atmospheres*, *111*(D10). https://doi.org/10.1029/2005JD006497

Thompson, D. W., Wallace, J. M., & Hegerl, G. C. (2000). Annular modes in the extratropical circulation. Part II: Trends. *Journal of Climate*, *13*(5), 1018–1036. https://doi.org/10.1175/1520-0442(2000)013<1018:AMITEC>2.0.CO;2

Thompson, D. W. J., & Solomon, S. (2002). Interpretation of recent Southern Hemisphere climate change. *Science*, *296*(5569), 895–899. https://doi.org/10.1126/science.1069270

Thompson, D. W. J., & Wallace, J. M. (1998). The Arctic oscillation signature in the wintertime geopotential height and temperature fields. *Geophysical Research Letters*, *25*(9), 1297–1300. https://doi.org/10.1029/98GL00950

Vavrus, S. J., Wang, F. Y., Martin, J. E., Francis, J. A., Peings, Y., & Cattiaux, J. (2017). Changes in North American atmospheric circulation and extreme weather: Influence of Arctic amplification and Northern Hemisphere snow cover. *Journal of Climate*, *30*(11), 4317–4333. https://doi.org/10.1175/JCLI-D-16-0762.1

Wallace, J. M., & Gutzler, D. S. (1981). Teleconnections in the geopotential height field during the Northern Hemisphere winter. *Monthly Weather Review*, *109*(4), 784–812. https://doi.org/10.1175/1520-0493(1981)109<0784:TITGHF>2.0.CO;2

Waugh, D. W., Sobel, A. H., & Polvani, L. M. (2017). What is the polar vortex and how does it influence weather? *Bulletin of the American Meteorological Society*, *98*(1), 37–44. https://doi.org/10.1175/BAMS-D-15-00212.1

Wrona, K. M., & Rohli, R. V. (2007). Seasonality of the northern hemisphere circumpolar vortex. *International Journal of Climatology*, *27*(6), 697–713. https://doi.org/10.1002/joc.1430

10.1029/2019EA000590

## Erratum

In the originally published version of this article, Figure 2 contained a minor typographical error. The figure has since been corrected, and this version may be considered the authoritative version of record.